Chapter 1
Silicon Photonic Wire Waveguides: Fundamentals and Applications

Koji Yamada

Abstract This chapter reviews the fundamental characteristics and basic applications of the silicon photonic wire waveguide. Thanks to its ultra-small geometrical structures and compatibility with the silicon electronics, the silicon photonic wire waveguide provides us with a highly integrated platform for electronic–photonic convergence. For the practical achievement of this platform, however, we must search for ways to reduce the propagation loss and coupling loss to external fibers and overcome the polarization dependence. Progress has been made by applying state-of-the-art technologies specially tuned to the fabrication of nanometer structures, and the fundamental propagation performance has already become a practical standard. Some passive devices, such as branches and wavelength filters, and dynamic devices based on the thermo-optic effect or carrier plasma effect have been developed by using silicon photonic wire waveguides. These waveguides also offer an efficient media for nonlinear optical functions, such as wavelength conversion. Although polarization dependence remains a serious obstacle to the practical applications of these waveguides, waveguide-based polarization manipulation devices provide us with effective solutions, such as a polarization diversity system.

1.1 Introduction

In recent years, silicon photonics has attracted attention as an emerging technology for optical telecommunications and for optical interconnects in microelectronics. Based on highly sophisticated silicon semiconductor technology, silicon photonics would provide us with an inexpensive highly integrated electronic–photonic platform, in which ultra-compact photonic devices and electronic circuits are converged.

Similar to the existing silica-based or III–V semiconductor-based photonic systems, silicon photonics also requires an optical waveguide system. The waveguide

K. Yamada (✉)
NTT Microsystem Integration Laboratories, NTT Corporation,
Atsugi, 243-0198 Japan
e-mail: kyamada@aecl.ntt.co.jp

D.J. Lockwood, L. Pavesi (Eds.): *Silicon Photonics II*.
Topics in Applied Physics **119**, 1–29 (2011)
DOI 10.1007/978-3-642-10506-7_1

must have features that allow us to accommodate passive and dynamic photonic devices such as wavelength filters and modulators. The waveguide system must also be flexible enough to allow active functions, such as light emission and detection to be implemented. Of course, it should guarantee a sufficiently low propagation loss for constructing and integrating these photonic functions. Furthermore, for monolithic electronic–photonic convergence, the most important advantage of silicon photonics, the following requirements must be met:

(1) Waveguides should be constructed on silicon substrates or be constructed together with silicon electronic devices.
(2) Waveguide fabrication processes should not damage electronic devices.
(3) Waveguides should not be damaged by the processes for fabricating electronic devices.
(4) Waveguide materials must not be hazardous to silicon electronics.
(5) Geometrical criteria, such as the layout of photonic devices, should not interfere with the electronic circuit layout.

These requirements are very difficult to meet with conventional waveguide systems. For example, the fabrication process for conventional silica-based waveguide requires high temperatures exceeding 1,000 °C, which would seriously damage electronic devices. Moreover, silica-based waveguides have a large bending radius on the order of millimeters or even centimeters, making it impossible to integrate photonic circuits on an electronic chip, whose typical size is a few centimeters square. The III–V compound semiconductor-based waveguides and photonic devices have geometries smaller than those in the silica-based system; however, on a silicon substrate it is very difficult to epitaxially grow the high-quality III–V materials needed for the construction of practical photonic devices. Etching and other fabrication procedures are completely different from silicon processes. Moreover, III–V material contamination must be eliminated from silicon electronics. At present, it is therefore very difficult to introduce III–V compounds into silicon electronics. Polymer waveguides made of organic materials cause less damage to electronic devices. However, their use is limited to the uppermost layers formed after the electronic circuits are completed or to other regions separated from the electronic devices because they cannot withstand the temperatures used in electronic device fabrication.

Recently, silicon oxynitride (SiON) and silicon nitride (Si_3N_4) waveguides have also been proposed as a compact waveguide system [1, 2]; however, these silicon nitride waveguides might be not suitable for electronic–photonic convergence for infrared light at wavelengths around 1,500 nm. Silicon nitride materials formed by low-temperature deposition methods generally contain N–H bond residues, which readily absorb infrared light at around 1,500 nm. A high-temperature (1,000 °C or more) annealing can reduce the absorption, but the high-temperature process is not compatible with electronic devices.

From the viewpoint of material, a silicon-based waveguide is obviously preferable for electronic photonic convergence. So far, several types of silicon waveguides have been proposed such as rib-type waveguides with core dimensions of a few micrometers [3, 4] and photonic wire waveguides with core dimensions of several

hundreds of nanometers [5–10]. The latter are especially promising for electronic–photonic convergence because their ultra-small core dimensions and micrometer bending sections match the dimensions of electronic circuits. The waveguides are constructed on silicon-on-insulator (SOI) substrates, where the uppermost SOI layer is used as the waveguide core so that there is no need to form the core material. The cladding material is a silica-based material formed by a low-temperature process such as plasma-enhanced chemical vapor deposition (PE–CVD) [11].

Besides the advantages of silicon photonic wire waveguides in electronic–photonic convergence, highly integrated ultra-compact photonic circuits based on photonic wire waveguides guarantee low power consumption and low packaging cost. Furthermore, the waveguides also offer advanced functionality through the use of its semiconductor characteristics of silicon.

1.2 Fundamental Design of Silicon Photonic Wire Waveguides

1.2.1 Guided Modes

A schematic of s silicon photonic wire waveguide is shown in Fig. 1.1a. The waveguide consist of a silicon core and silica-based cladding. The core dimension should be determined so that a single-mode condition is fulfilled. The single-mode condition is very important in constructing practical functional devices because whether or not we can implement a desired function depends on the fundamental guided mode. The core dimension of single-mode silicon photonic wire waveguides is significantly smaller than that of conventional single-mode silica waveguides. In the waveguide system consisting of a silicon core and silica claddings, the refractive

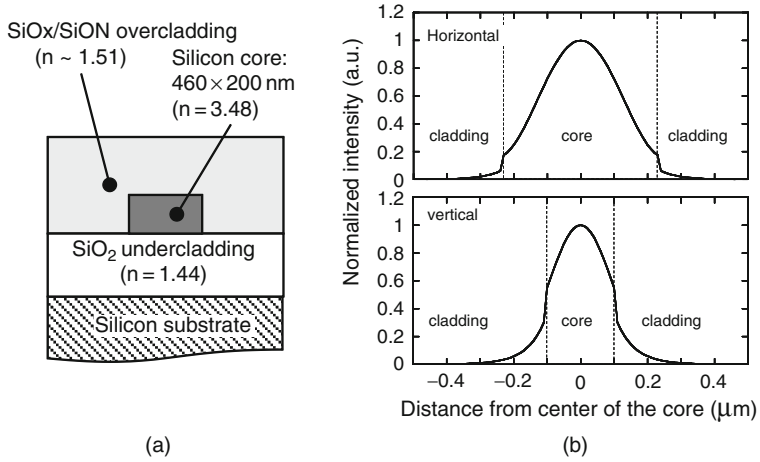

Fig. 1.1 (**a**) Cross-sectional structure and (**b**) optical intensity distribution of a typical silicon photonic wire waveguide

index contrast Δ between the core and cladding is as large as 40%, which allows a total internal reflection with a very large incident angle of 60°. This situation is similar to that in metallic rectangular waveguides, whose waveguide dimensions are smaller than or comparable to a half-wavelength of the guided electromagnetic waves. In silicon photonic wire waveguides, therefore, the core dimension that fulfills a single-mode condition should also be smaller than or comparable to a half-wavelength of a guided wave in silicon. Since the refractive index of silicon is about 3.5 for photon energies below the band-gap energy, the core dimension of a silicon photonic wire waveguide should be less than or comparable to 400 nm for 1,310∼1,550-nm telecommunications-band infrared light. Generally, the core shape is made flat along the substrate to reduce the etching depth in practical fabrications. In many cases, the height of the core is typically half of the width. Thus, a typical core geometry is a 400 × 200-nm^2 rectangle.

A detailed analysis of the guided modes can be performed by various numerical methods such as the finite difference method (FDM) [12], finite element method (FEM) [13], and film mode matching method (FMM) [14]. Figures 1.2a and b show calculated effective indices n_{eff} of guided modes for 1,550-nm infrared light in various core geometries. Calculations were performed by the FMM and the indices of silicon and silica were set at 3.477 and 1.444, respectively. The mode notations are taken from [15], in which E^x and E^y modes represent the transverse electric (TE)-like and transverse magnetic (TM)-like modes, respectively. As shown Fig. 1.2a for waveguides of 200-nm silicon thickness, single-mode conditions are fulfilled when the core width is less than 460 nm for TE-like guided modes in which the dominant electric field is parallel to the substrate. The mode field profile of the TE-like fundamental mode is shown in Fig. 1.1b for a 460 × 200-nm^2 core. For a TM-like mode in which the dominant electric field is perpendicular to the substrate,

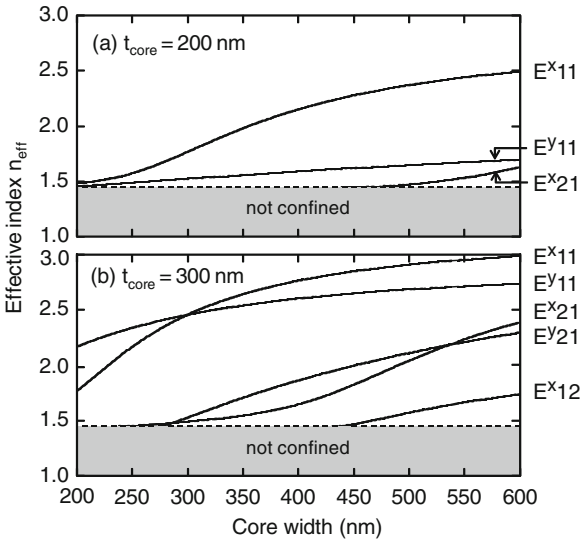

Fig. 1.2 Core width dependence of the effective indices of silicon photonic wire waveguides

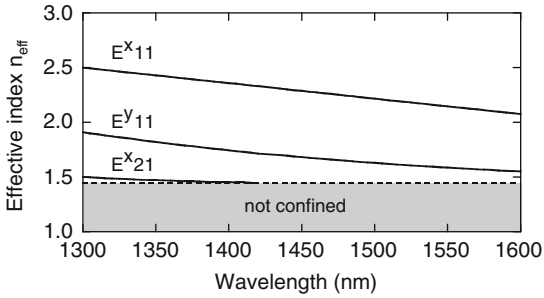

Fig. 1.3 Wavelength dependence of the effective indices of silicon photonic wire waveguides

the single-mode condition is fulfilled in a core larger than that for the TE-like mode. The effective indices of TE and TM fundamental modes show a large difference. In other words, the 200-nm-thick flat core produces a large polarization dependence. For waveguides with 300-nm-thick silicon as shown in Fig. 1.2b, core widths satisfying single-mode conditions are smaller than those for 200-nm-thick silicon. In a 300-nm^2 core, the refractive indices are identical for the TE and TM fundamental modes: that is, the polarization dependence can be eliminated.

Figure 1.3 shows the calculated wavelength dependence of the effective refractive indices for the waveguides with a 400×200-nm^2 core. Calculations were performed by the FMM and the material dispersions of refractive indices were considered. As shown in Fig. 1.3, the single-mode condition is violated in the wavelength region below 1,420 nm for the TE-like mode. For the 1,310-nm telecommunications wavelength band, therefore, a smaller core should be used for satisfying the single-mode condition.

1.2.2 Effect of Geometrical Errors and Birefringence

As shown in Fig. 1.2, the effective indices of silicon photonic wire waveguide are extremely sensitive to the core geometries. The group index n_g, which is an essential parameter in designing delay-based devices such as optical filters, is also affected significantly by the core geometry. Figures 1.4a and b show calculated group indices and their sensitivities to the core width $dn_g/n_g dw$. For TE-like modes, for which most of the photonic functions are designed, the sensitivities to the core width $dn_g/n_g dw$ are around 2×10^{-4} nm^{-1} for a 400×200-nm^2 core and much higher for a 300-nm^2 core. For wavelength filters for dense wavelength division multiplexing (DWDM), the group index should be controlled to on the order of 1×10^{-4} or less. The index restriction corresponds to a core width accuracy of 0.5 nm or less, which is essentially unattainable with current micro-fabrication technology. Fortunately, there are optimum geometries giving very low sensitivities to the core width. For example, 385×200-nm^2 and 325×300-nm^2 cores are robust against the errors in core width. Waveguides with a very wide core are also robust against the errors in core width. In an arrayed waveguide grating (AWG) filter, waveguides with 750×200-nm^2 cores are used to reduce phase errors due to the variation of

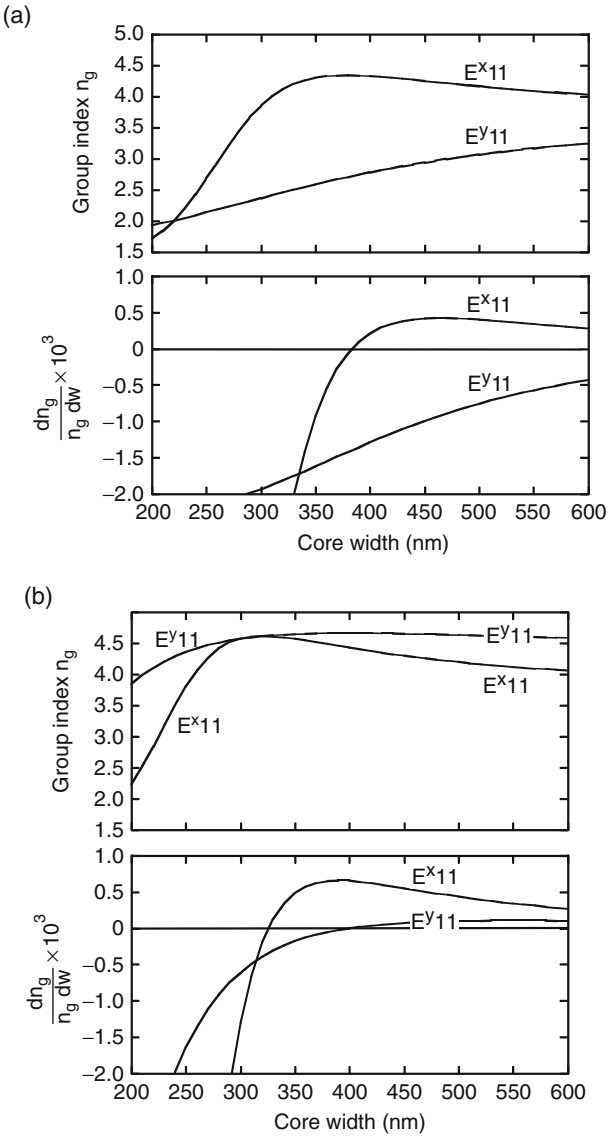

Fig. 1.4 (**a**) Core width dependence of the group indices and their derivatives for waveguides with 200-nm-thick cores (**b**) Core width dependence of the group indices and their derivatives for waveguides with 300-nm-thick cores

core width [16]. When we use such a wide-core waveguide, however, higher order modes stimulated in bending and other asymmetric structures become a concern.

Figure 1.4 also that the structural birefringence is incredibly large and that the problem of the polarization dependence in a silicon photonic wire waveguide is practically unsolvable. In a waveguide with a 400×200-nm^2 core, the group indices are 4.33 for the TE-like fundamental mode and 2.78 for the TM-like fundamental

mode. The difference in the group indices gives a polarization mode dispersion (PMD) of 51.7 ps/cm, which seriously limits the applicable bandwidth in high-speed data transmission. The polarization-dependent wavelength (PDλ) in delay-based filter devices, such as AWGs and ring resonators, would be incredibly large. A square core would not be a solution to this problem because the group index is very sensitive to the core geometry, as mentioned before. In other words, polarization diversity is necessary for eliminating the polarization dependence in photonic devices based on silicon photonic wire waveguides.

1.2.3 Propagation Loss and Radiation Loss in Bending

The intrinsic loss in undoped silicon is very low for the photon energies below the band gap (∼1.1 eV); therefore, the propagation loss of photonic wire waveguides is mainly determined by scattering due to surface roughness of the core. The effect of the surface roughness on the scattering loss in dielectric waveguides has been theoretically studied and formulated by Payne and Lacey [17]. The formula is represented by a complicated function characterized by a root-mean square roughness σ and the correlation length of the surface roughness structure l_c; the upper bound of the scattering loss α_{max}, as given in [18], is shown below.

$$\alpha_{max} = \frac{\sigma^2 \kappa}{k_0 d^4 n_1}, \tag{1.1}$$

where, k_0, d, and n_1 are wavevector of the light in vacuum, the half-width of the core, and effective index of a silicon slab with the same thickness as the core, respectively. The factor κ depends on the waveguide geometry and the statistical distribution (Gaussian, exponential, etc.) of the roughness, in which the correlation length l_c is included. According to [17], κ is on the order of unity for most practical waveguide geometries. Thus, the scattering loss is inversely proportional to the fourth power of d. In other words, it will seriously increase in photonic wire waveguides with an ultra-small core. A roughness of only 5 nm, for instance, would cause a 60-dB/cm scattering loss in a 400-nm-wide core made of a 200-nm-thick silicon slab whose effective index is 2.7. To achieve a practical scattering loss of a few decibels per centimeter, the surface roughness should be about 1 nm or less.

Radiation losses in the bending section can be calculated by applying cylindrical coordinates in numerical mode solvers. Figure 1.5 shows calculated radiation losses for a 90° bend in various waveguides. The calculations were performed by using a commercially available FMM mode solver [19]. As shown in this figure, the bending performance varies with polarization. For the TE-like mode in the waveguide with a 400×200-nm^2 core, the radiation loss is negligible even if the bending radius is as small as 2.5 μm. For the TM-like mode, however, a bending radius of over a few tens of micrometers is needed in order to achieve negligible radiation loss. The bending loss also varies with core dimensions. As shown in Fig. 1.5, for TE-like modes, a waveguide with a 300-nm^2 core requires a larger bending radius than a flat waveguide.

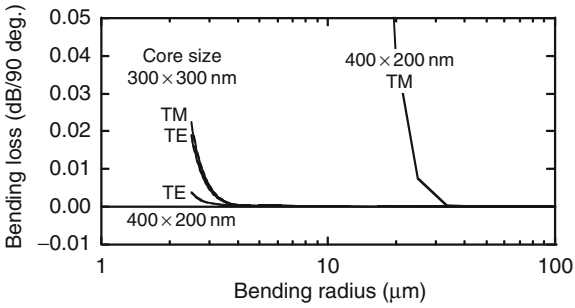

Fig. 1.5 Calculated radiation losses for a 90° bend in various waveguides

1.2.4 Coupling to External Fiber

Since a silicon photonic wire waveguide has a very small mode profile, spot-size conversion is essential for connecting it to external circuits such as single-mode optical fibers. A highly efficient spot size converter (SSC) with a silicon reverse adiabatic taper has already been proposed [20]. As shown in Fig. 1.6, it has a double-core structure consisting of a thin silicon taper and silica-based waveguides. In a typical design for 1,550-nm-wavelength infrared light, the tip of the taper should be ultimately reduced to less than 100 nm and the silica-based waveguide has a 3-μm^2 core with a 2.5% index contrast to the cladding. In such a double-core structure, light leaking from the silicon taper is captured by a silica-based waveguide, which guarantees efficient optical coupling to external optical fibers.

Figure 1.7 shows the calculated conversion efficiencies between a silicon photonic wire waveguide with a 400 × 200-nm^2 core and a silica-based waveguide with a 3-μm^2 core. As shown in this figure, a 200-μm-long taper with a 80-nm tip gives a conversion loss of around 0.1 dB for both polarizations. A shorter and thicker taper would give lower coupling efficiencies. Since the coupling loss between a silica-based waveguide with a 3-μm^2 core and a high-numerical-aperture (NA) fiber with a 4.3-μm mode field diameter is about 0.1 dB and the conversion loss between

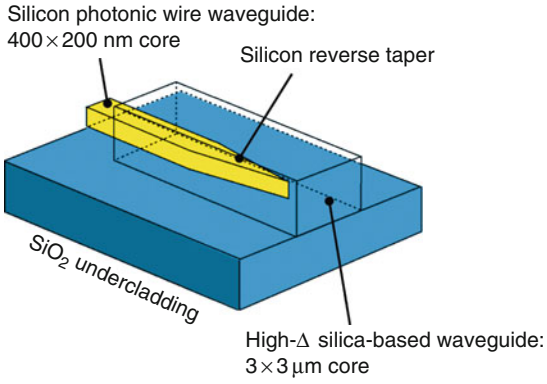

Fig. 1.6 Schematic of the spot size converter

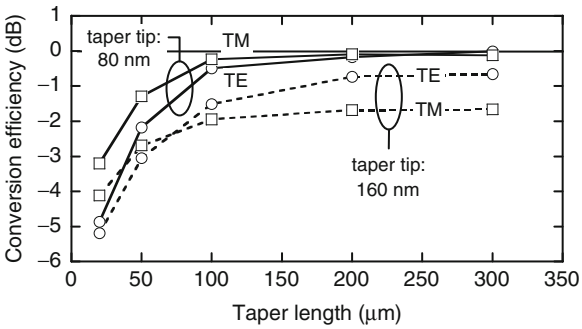

Fig. 1.7 Calculated conversion efficiencies in spot size converters with various geometries

the high-NA fiber and the ordinary single mode can be reduced to about 0.1 dB by applying a thermally expanded core (TEC) technology [21], a total coupling loss of less than 0.5 dB can be achieved between a photonic wire waveguide and a single-mode fiber.

A grating coupler input/output structure has also been proposed [22], for which the coupling efficiency between a photonic wire waveguide and an ordinary single-mode fiber is calculated to be −5 to −3 dB.

1.3 Fundamental Propagation Performance

1.3.1 Fabrication

Figure 1.8 shows a typical fabrication process for a Si-wire waveguide. First, a hard mask layer and resist mask layer are formed on a SOI substrate. The hard mask is used to improve the selectivity of Si etching and is often made of SiO_2. Next, waveguide patterns are defined by using electron beam (EB) lithography or excimer laser deep ultraviolet (DUV) lithography [9], which are capable of forming 100-nm patterns. Ordinarily, EB and DUV lithography technologies are used in the fabrication of electronic circuits where they are optimized for patterning of straight and intersecting line patterns. Therefore, no consideration has been given to curves and roughness in the pattern edges, which are important factors in fabricating low-loss optical waveguides. To reduce propagation losses of the waveguides, it is necessary to reduce the edge roughness to around 1 nm or less. This means that particular care must be taken in the data preparation for EB shots or DUV masks. Figure 1.9 shows an ultra-small ring resonator with and without special treatment for EB data preparation, where a drastic reduction in side-wall roughness is observed as a result of the special treatment [23]. The writing speed of the EB lithography must also be considered in practical fabrication. For practical purposes, it is probably necessary to use EB lithography with a variable-shaped beam.

After resist development and SiO_2 etching for a hard mask, the silicon core is formed by low-pressure plasma etching with an electron-cyclotron resonance (ECR) plasma or inductive coupled plasma. To ensure the edge roughness of the side walls

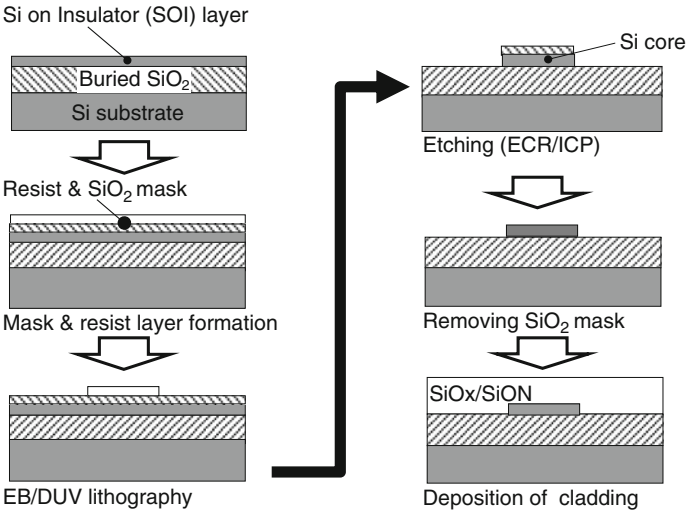

Fig. 1.8 Typical fabrication process of a silicon photonic wire waveguide

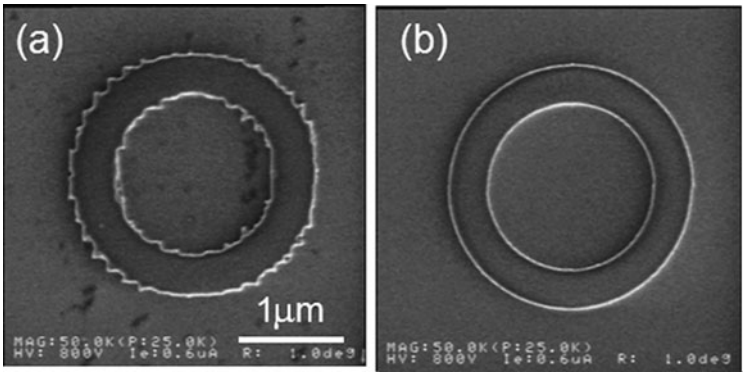

Fig. 1.9 SEM images of ring resonators (**a**) without and (**b**) with EB data optimizations

is at sub-nanometer levels, the plasma conditions and the selection of etching gases must be tuned for individual plasma equipment.

Finally, an overcladding layer is formed with a SiO_2-based material or polymer resin material. To avoid damaging the silicon layer, the cladding layers must be deposited by a low-temperature process, such as the plasma-enhanced chemical vapor deposition (PE–CVD) method [11]. In particular, for waveguides associated with electronic structure, it is essential to use a low-temperature process so as not to damage the electronic devices.

Figure 1.10a shows a scanning electron microscope (SEM) image of the core of a silicon photonic wire waveguide with a cross-section of $400 \times 200\,\mathrm{nm}^2$ [8]. The geometrical shape closely matches the design values, and the perpendicularity of the sidewalls is also very good. Figure 1.10b shows a photograph of the 80-nm-wide

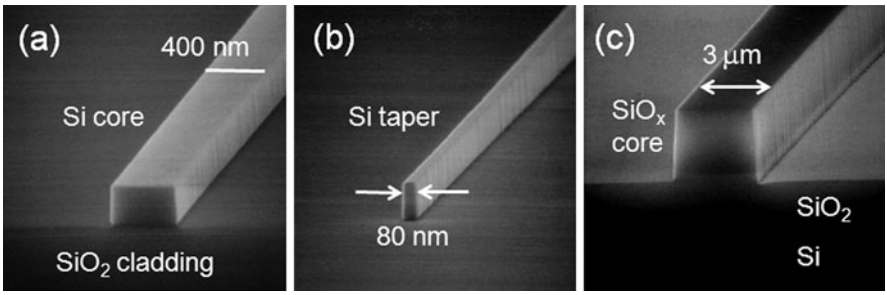

Fig. 1.10 SEM images of a silicon photonic wire waveguide system. (**a**) Core of silicon photonic wire waveguide, (**b**) silicon taper, and (**c**) core of SiOx waveguide for spot size converter

taper tip in the SSC. The taper and waveguide core were constructed by using a common fabrication process. Figure 1.10c shows an SEM photograph of the core of the silica waveguide for the SSC. The silica waveguide core was fabricated by depositing SiO_2-based material by the PE–CVD method and etched by reactive ion etching (RIE). By adjusting the deposition conditions, the refractive index of the material is tuned to be 2.5% higher than that of an ordinary thermal oxide. In the final product, a 7-μm SiO_2 overcladding layer covers the whole structure.

1.3.2 Propagation Performance

Figure 1.11 shows a typical transmission loss of silicon photonic wire waveguides with SSC, fabricated in the manner mentioned above. High-NA optical fibers with 4.3-μm mode field diameter (MFD) are used for external coupling. As shown in this figure, the propagation loss for the TE-like mode has been improved to be around 1 dB/cm. In the waveguide with flat cores, the propagation losses for TM-like modes are generally better than those for TE-like modes. Oxidation of the core sidewalls may further reduce the propagation losses [24]. The propagation loss of around 1 dB/cm is already at a practical level, since photonic devices based on silicon photonic wire waveguides are typically smaller than 1 mm. Besides the sidewall

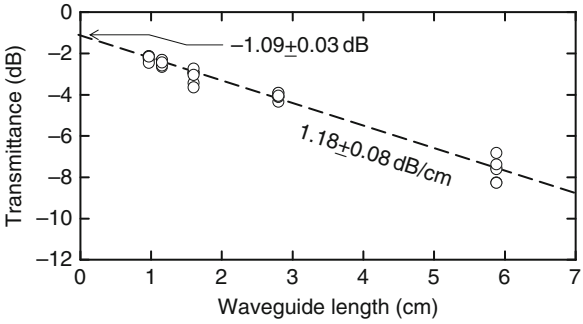

Fig. 1.11 Measured propagation loss of a silicon photonic wire waveguide with spot size converters

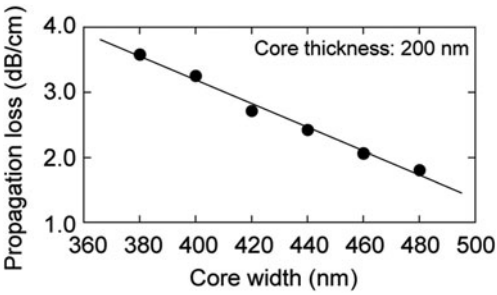

Fig. 1.12 Relation between measured propagation losses and core width

roughness of the core, the core width affects propagation losses as well. Figure 1.12 shows the relation between measured propagation losses and core widths. As shown, the propagation loss is reduced by increasing the core width because the effect of sidewall roughness is reduced in a wide core. When the core width exceeds 460 nm, the waveguide can also guide a higher order mode which may degrade the performances of some photonic devices.

The coupling loss between optical fiber and silicon photonic wire waveguide is represented by the intercept of the vertical axis in Fig. 1.11. The loss value at the intercept includes two waveguide/fiber interfaces; therefore in this case, one interface has a 0.5 dB coupling loss at a wavelength of 1,550 nm.

Figure 1.13 shows the transmission spectrum of a silicon photonic wire waveguide with SSCs. The spectrum remains flat over a 200-nm wide bandwidth, and no absorption dip is observed. The flat spectrum means that the SiO_2-based material used in the SSC does not contain impurities with N–H bonds. Although absorption by residual O–H bonds exists at wavelengths of around 1,400 nm, the resulting losses are not large. It is also possible to eliminate O–H bonds by heat treatment.

Figure 1.14 shows bending losses of single mode waveguides for TE-like modes. For the bending radius of over 5 μm, bending losses are negligible. Even for an ultra-small bending radius of around 2 μm, a waveguide with a flat core maintains

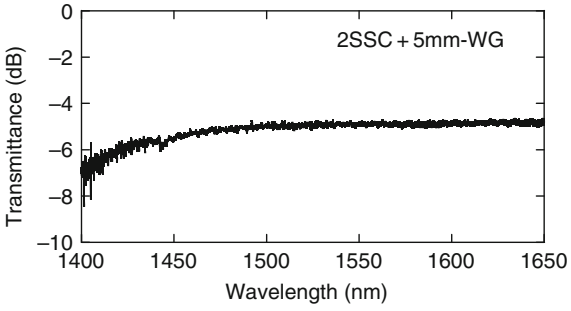

Fig. 1.13 Measured transmission spectrum of a typical silicon photonic wire waveguide with spot size converters

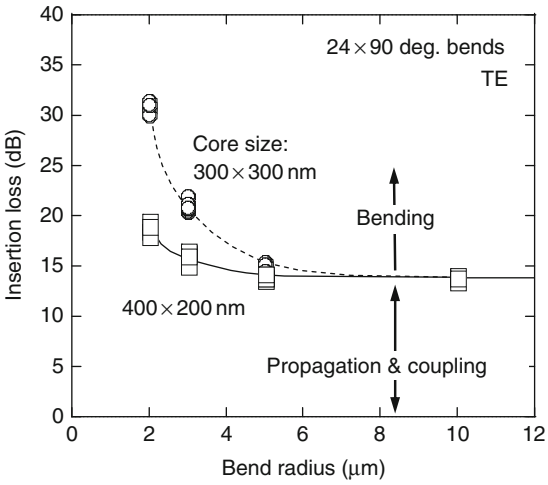

Fig. 1.14 Relation between measured insertion losses of the waveguides and bending radius

a low loss of below 0.1 dB per 90° bend. A waveguide with a square core shows a larger bending loss for a bending radius below 5 μm. For TM-like modes, especially in waveguides with flat cores, bending losses are generally larger than those for TE-like modes. Bending losses measured in various research groups are summarized in [10].

The birefringence of the waveguide can be evaluated by the free spectral ranges (FSRs) of ring resonators. Figure 1.15 shows measured transmission spectra at around 197 THz ($\lambda = 1.514\,\mu$m) for a ring resonator of 10-μm radius. In this figure, the FSR in TM-like modes (1.67 THz) is significantly larger than that in TE-like modes (1.11 THz). Using the FSR, we can roughly express the group index of the waveguide by $n_g = c/2\pi R\Delta f$, where c, R, and Δf are the speed of light in a vacuum, the radius of the ring resonator, and the FSR in hertz, respectively. Thus, the group indices are estimated to be 4.30 and 2.86 for TE and TM modes, respectively, which agree well with the design values in the previous section.

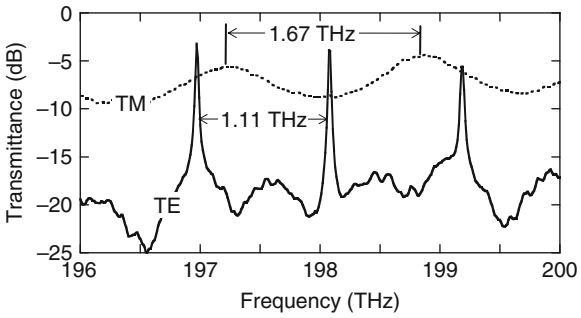

Fig. 1.15 Measured drop port spectra of a ring resonator with 10-mm radius

1.4 Simple Applications of Silicon Photonic Wire Waveguides

1.4.1 Passive Devices

The simplest passive device is a branch. Various branching devices, such as a Y branch and a multimode interference (MMI) branch, have been proposed and fabricated with silicon-wire waveguides [6, 7]. Figure 1.16a shows a multi-stage branch implemented with MMI branches [25]. The MMI branch units are no more than 3 μm in size, and the waveguides can bend light with a micrometer radius, so it is easy to configure multi-stage branches in a small area. Figure 1.16b shows the transmittance of the cascaded MMI branches for each output port. The transmittance linearly decreases with respect to the branching order. In other words, the branches of each stage are fabricated with uniform quality.

Compact add/drop wavelength filters are also being developed by using the ultra-compact bending parts of silicon-wire waveguides. Various ring-resonator-based filters have been developed. A single resonator is very compact and suitable for high-density integration; however, its Lorentzian resonance, as shown in Fig. 1.15, is not suitable for filters for telecommunications applications, which require flat pass bands. For a flat pass band, cascaded ring resonators have recently been developed [26].

Complex wavelength filters, such AWG filters [16, 27] and the lattice filters [28, 29], have also been developed. A photograph of a lattice filter is shown in Fig. 1.17a. In such filters, the pass-band spectrum can be fine-tuned by applying various optimization techniques, such as apodization. As shown in Fig. 1.17b, for

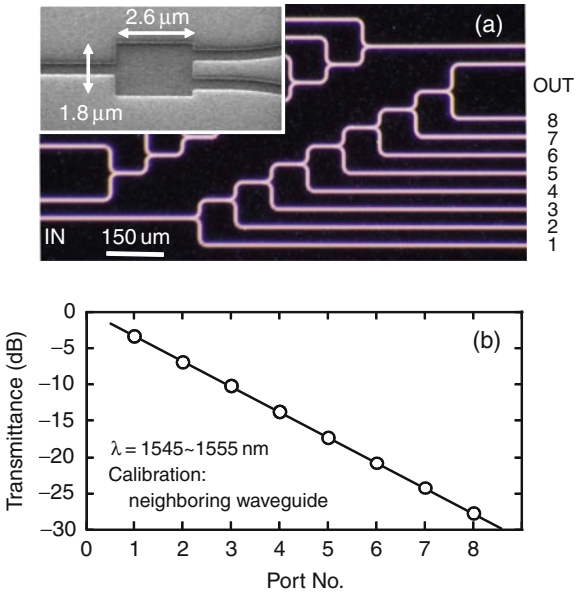

Fig. 1.16 (**a**) Cascaded MMI branches and (**b**) their transmission characteristics

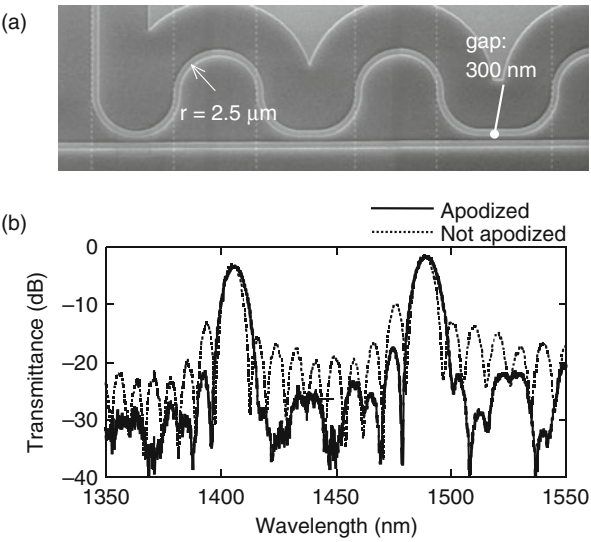

Fig. 1.17 (**a**) A SEM photograph of a part of a lattice filter and (**b**) measured drop port spectra

example, adjacent channel crosstalk is reduced to be about −20 dB in the lattice filters for which apodization of the coupling coefficients in the directional couplers has been performed [29]. The shape of the pass band could also be controlled by apodization in these sophisticated filters.

Wavelength tuning and polarization dependence are serious obstacles to the practical applications of these wavelength filters. As shown in the previous sections, effective indices of silicon photonic wire waveguides are extremely sensitive to geometrical errors in the core shape. The indices are also sensitive to the environmental temperature. Therefore, index tuning by temperature control or carrier injection is necessary for fixing the pass band to a certain wavelength. As described in the previous sections, the structural birefringence is also very sensitive to the core geometry, and it is virtually impossible to eliminate the polarization dependence of passive devices based on silicon photonic wire waveguides. A practical solution for the polarization dependence is the polarization diversity, whose details are described in Sect. 1.5.

1.4.2 Dynamic Devices

1.4.2.1 Thermo-optic Effect

The thermo-optic (TO) effect in silicon is ten times or more stronger than that in silica [30] and the volume of the core in silicon photonic wire waveguides is smaller than that of the core in silica-based waveguides. Therefore, power consumption in silicon-based TO devices can be one-tenth of that in silica-based devices. To achieve such a low power consumption, it is very important to concentrate the heating power in the waveguide core. However, heat expansion in the thick (∼3 μm) and laterally

wide cladding layer is an obstacle to the heat convergence. In the early applications of the TO effect in optical switches based on Mach-Zehndar interferometers (MZIs), heaters were constructed on a thick overcladding without lateral thermal insulation. In such TO switches, a few tens of milliwatts of heater power is necessary for a π phase shift in one arm of a MZI [11]. Compared to typical silica-based TO switches, silicon-based devices without an efficient heating structure do not show a remarkable improvement in power consumption. Recently, a very efficient heating structure has been proposed. Figure 1.18 shows a cross-sectional schematic of the heating structure. In the heating structure, the undercladding and side-cladding are removed and only a several-micrometer-wide silica cladding containing a silicon core is supported by thin silica beams [31]. By applying this structure as a phase shifter in MZIs, the heating power has been reduced to be less than 1 mW, as shown in Fig. 1.19, which is about 1/100th of that of conventional silica-based TO switches.

1.4.2.2 Carrier Injection

In the infrared and visible regions, the optical properties of silicon are affected by free carriers, especially for photon energies below the band gap (~1.1 eV). By applying the Drude approximation and assuming the carrier plasma frequency is

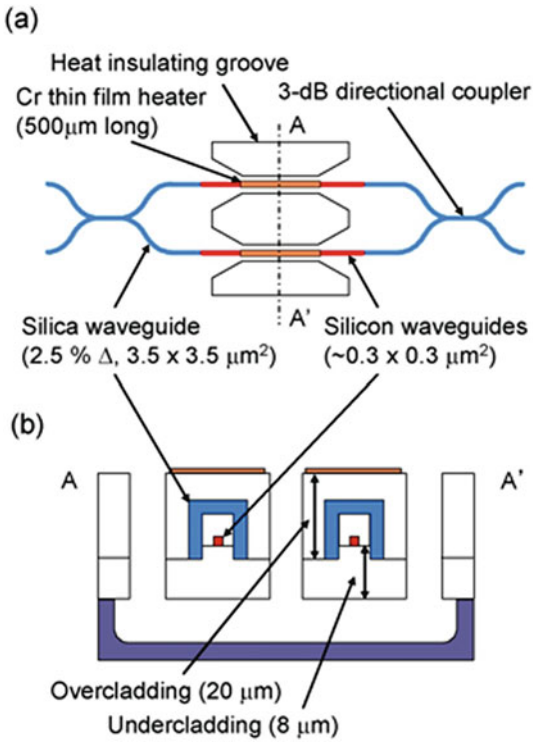

Fig. 1.18 Schematic structure of the low power consumption switch: (**a**) Top view and (**b**) cross-sectional view along line A–A′ in (**a**) [31]

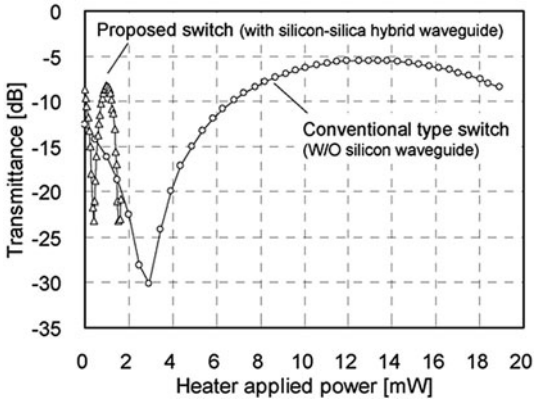

Fig. 1.19 Switching characteristics of low-power and conventional switches for TE polarization [31]

significantly lower than the optical frequency, the changes of refractive index Δn and absorption coefficient $\Delta\alpha$ are expressed by the following formulas [32]:

$$\Delta n = \frac{-e^2\lambda^2 N}{8\pi^2 c^2 \varepsilon_0 n m^*} \tag{1.2}$$

$$\Delta a = \frac{e^3\lambda^2 N}{4\pi^2 c^3 \varepsilon_0 n \mu m^{*2}} \tag{1.3}$$

where e, c, ε_0, and n are the elementary charge, the speed of light in a vacuum, the vacuum permittivity, and the refractive index of silicon, respectively. N, m^*, and μ are the injected carrier density, the carrier effective mass, and carrier mobility, respectively.

To control the concentration of free carriers in the waveguide core, silicon photonic wire waveguides with a p-i-n carrier injection structure have been developed [33–35]. A Typical cross-section of a waveguide with a p-i-n carrier injection structure is shown in Fig. 1.20a. The typical core size of waveguides with a p-i-n structure is 400–600 × 200 nm^2. At both sides of the core, the waveguide has slab regions for carrier injection. Although the core shape resembles that of conventional silicon rib waveguides [3], its geometrical size is far smaller than in the conventional ones. Moreover, the bending radius is less than a hundredth of that in conventional rib waveguides. These reductions in geometries are greatly advantageous for applications of silicon photonic wire waveguides with the carrier injection structures. For example, the device length would be significantly reduced because the carrier concentration can be increased in an ultra-small core. In such a short device with an ultra-small core, the electric power consumption can be significantly reduced. Moreover, the operation speed can also be increased because a small core guarantees a fast carrier transit time.

By applying these advantages of silicon photonic wire waveguides with p-i-n structures, various dynamic devices, such as high-speed modulators [33, 35] and variable optical attenuators (VOA) [34], have been developed. Among them, in this section, the application of the p-i-n carrier injection structure to a VOA is described.

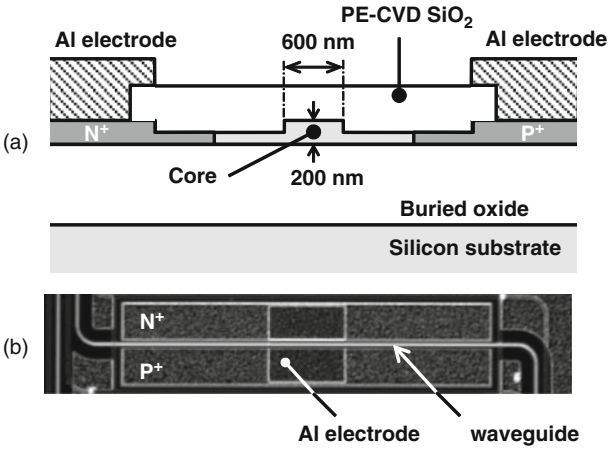

Fig. 1.20 (**a**) Cross-sectional view and (**b**) top view of a silicon photonic wire-based carrier injection structure

As show in Fig. 1.20a, the waveguide is a rib-type one with a $600 \times 200\text{-nm}^2$ core and 100-nm-thick slab. This structure satisfies the single-mode condition for 1,550-nm infrared light. The slab is thicker than those reported in [33] and [35]. The thick slab is important for reducing propagation loss and device impedance.

The core was fabricated in same manner as for passive waveguides. After thermal oxidation for surface passivation, the n^+ and p^+ regions were defined in the slab section by lithography and implanted with phosphorus and boron as dopants. After annealing for the activation and diffusion of dopants, a silicon dioxide layer was deposited. The dopant density was about $10^{20}\ \text{cm}^{-3}$ in each doped region. Aluminum electrodes were then constructed on the doped regions.

Figure 1.20b shows a fabricated waveguide with the carrier injection structure in which the pair of contact electrodes can be seen. The propagation loss is typically less than 2 dB/cm. Figure 1.21 shows typical electrical characteristics of a 1-mm-long carrier injection structure. In spite of the device length, the reverse current is very low, around pico-amperes. This means the leakage of the device is small, so that injected carriers will effectively interact with guided light.

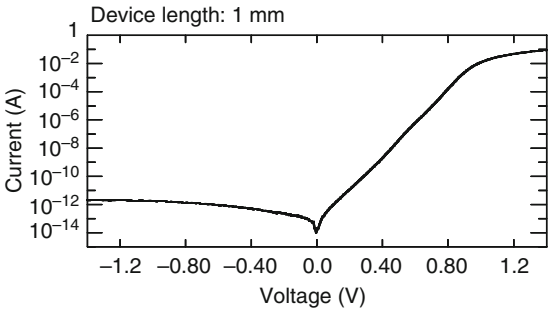

Fig. 1.21 Measured current-voltage relation of the carrier injection structure

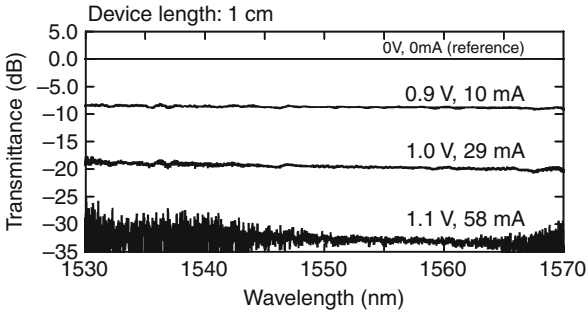

Fig. 1.22 Measured transmission characteristics of the variable optical attenuator

By injecting carriers into the core, optical attenuation is performed through the free carrier plasma effect mentioned above. Figure 1.22 shows transmission spectra of a 10-mm-long waveguide for various injected currents. As the injected current increases, guided light is absorbed by the injected carriers. The wavelength dependence of the attenuation is very flat in the measured 40-nm bandwidth. Operation with a 30-dB attenuation requires a power of about 55 mW, which is about a half of the power consumption of conventional rib-type devices [34]. The power consumption can be reduced by a series connection of the devices, which is a similar to the technique used in conventional devices. Figure 1.23 shows the temporal response of optical attenuation in a 1-mm-long device with a 10-ns injection pulse. In a 2-V reverse bias operation, the response time is about 2 ns, which is about 100 times faster than that in conventional devices [34].

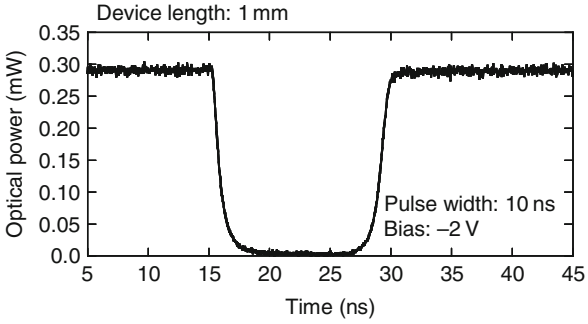

Fig. 1.23 Measured temporal response of the variable optical attenuator

Considering the linear propagation loss of the waveguide with the carrier injection structure, the on-chip insertion loss is estimated to be 2 dB in a 10-mm device and 0.2 dB in a 1-mm one. These values can satisfy required practical standards.

1.4.3 Nonlinear Functions

In addition to its use as a platform for passive and dynamic functions, a silicon photonic wire waveguide is also a promising platform for active functions based on

various nonlinear effects. Generally, bulk silicon shows weak nonlinearities. In silicon photonic wire waveguides, however, the optical power density can be increased in their ultra-small cores and nonlinear effects can be remarkably enhanced. The typical core size of the waveguide is 400–500 × 200 nm^2 at 1,550-nm wavelength, and the effective mode-field area A_{eff} is around 0.05 μm^2 [36]. Thanks to the ultra-small effective area, the Kerr nonlinear coefficient γ in silicon photonic wire waveguides is thus estimated to be 10^5–10^6 $(W\ km)^{-1}$. This value is about a hundred-thousand times larger than that for a single-mode dispersion-shifted fiber (DSF), which is a widely used media for nonlinear optics experiments. In other words, a centimeter-long silicon photonic wire waveguide is equivalent to a 100-m long DSF, giving practical efficiencies in various nonlinear functions. Although the interaction length and efficient power injection have been obstacles to obtaining practical efficiencies, the propagation loss of the waveguides has recently been improved to be 1–2 dB/cm and the coupling loss to external fibers has been reduced to be 0.5 dB by using a special SSC [20]. Thus, a power density of around 300 MW/cm^2 could be attained using commercially available 20-dBm CW light sources. The power density is high enough to obtain efficient nonlinear functions.

By applying the enhancement of nonlinear effects in a silicon photonic wire waveguide, various nonlinear functions, such as all-optical modulation based on the two photon absorption (TPA) effect [37], wavelength conversion and parametric amplification based on four wave mixing (FWM) effects [36, 38, 39] and stimulated Raman scattering (SRS) [4, 40], have been tested. Very recently, entangled-photon-pair creation has also been tested by using spontaneous FWM [41–43].

Among these functions, FWM-based wavelength conversion is here described as a typical nonlinear function giving an efficiency comparable to that in conventional devices [38]. The experimental setup for the wavelength conversion is shown in Fig. 1.24. A signal light with 10-Gbps non-return-to-zero (NRZ) modulation and a CW-operated pump light were injected collinearly into a 2.8-cm-long waveguide with SSCs. The polarization was adjusted to a TE-like mode, and the propagation loss of the waveguide was about 2.3 dB/cm. At the waveguide's entrance, the pump

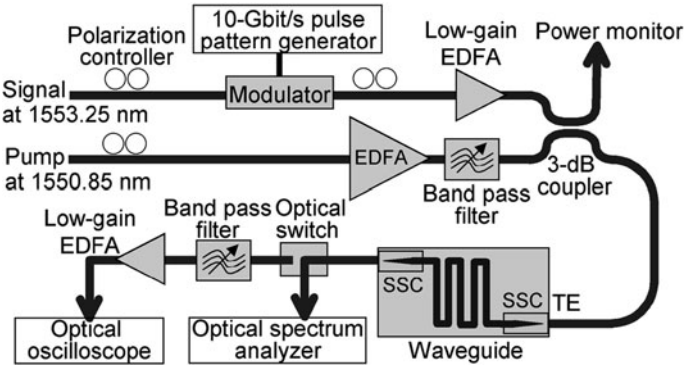

Fig. 1.24 Experimental setup for wavelength conversion using the four-wave mixing effect

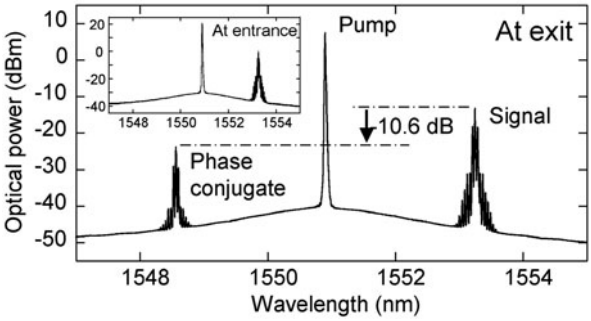

Fig. 1.25 Experimental result of wavelength conversion using the four-wave mixing effect

power was 160 mW CW, which gives a power density of around 430 MW/cm^2 in the waveguide.

The output spectrum at the exit of the waveguide is shown in Fig. 1.25. Besides the peaks of the injected pump and signal light, a peak of the phase conjugated light, or converted light, can be seen in the spectrum. The internal conversion efficiency is around −10 dB [38], which is comparable to that observed in periodically poled $LiNbO_3$ devices a few years ago [44], and large enough for practical data processing. As shown in Fig. 1.26, clear eye patterns of a 10-Gbps pseudorandom binary sequence (PRBS) data stream are observed in the converted light. The bandwidth giving a −3-dB efficiency degradation was measured to be over 20 nm [36]. The bandwidth was limited by the phase mismatching among waves. In silicon photonic wire waveguides, waveguide dispersion can be easily controlled by adjusting the core shape; therefore, the bandwidth could be further improved [39].

The conversion efficiency with respect to the pump power is shown in Fig. 1.27. Efficiency saturation due to the free carrier absorption effect can obviously be seen. The free carriers are generated through the TPA effect whose efficiency is proportional to the second power of the optical power density. Therefore, the simplest way to eliminate FCA is to reduce the power density. A theoretical estimation shows that a waveguide with 0.5-dB/cm propagation loss (dashed line) would provide an efficiency of −4 dB even if the pump power were 80 mW, where FCA is well suppressed [38]. Carrier sweep-out using a p-i-n structure, such as described in the previous section, is also a promising way to prevent FCA.

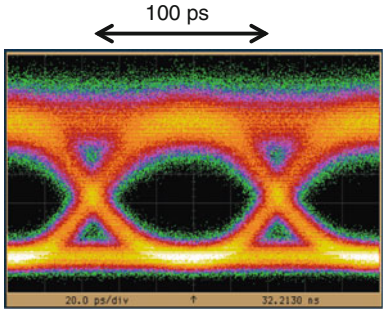

Fig. 1.26 Eye pattern of the signal of phase conjugated light

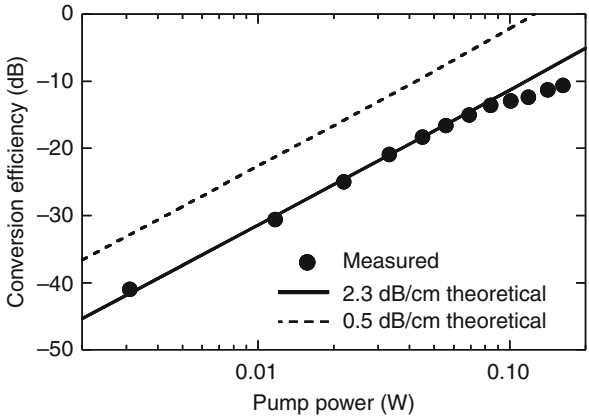

Fig. 1.27 Internal conversion efficiency versus pump power in wavelength conversion. The *dots* represent experimental results. The *solid* and *dashed lines* are theoretical estimations under the same conditions as those in the experiment except for propagation losses

1.5 Polarization Manipulation

As described in Sect. 1.2, the polarization dependence is one of the most serious obstacles to the practical application of silicon photonic wire waveguides, and polarization diversity is a unique solution to this problem. Generally, polarization diversity is achieved by using polarization splitters and rotators. If TE-like and TM-like modes can be separated by polarization splitters, and the TM-like modes can be converted into TE-like ones by rotators, we need only consider optical functions for the TE-like modes, not for both components. Thus, the polarization dependence could be eliminated by using a single-polarization (TE) platform. Such a polarization diversity system might be constructed by using free-space optical devices and optical fibers; however, this would require too much area and would be costly. For the polarization diversity circuit to be practical, it should be monolithically constructed on a chip. Recently, two types of on-chip polarization diversity circuits have been proposed [45, 46]. One is based on a two-dimensional grating coupler [45]. The other is based on a polarization splitter and rotator with silicon photonic wire waveguides [46]. Details of the latter are described in this section.

1.5.1 Polarization Splitter and Rotator

A scanning-electron micrograph of the fabricated polarization splitter is shown in Fig. 1.28. This device is based on a simple directional coupler with silicon photonic wire waveguides [47]. The coupling length for the TM-like modes is much shorter than for the TE-like modes. Thus, the TM-like modes can traverse the coupler, whereas the TE-like modes propagate along the initial waveguide. In a design for 1,550-nm infrared light, a directional coupler consisting of 200-nm-high and 400-nm-wide cores with a 480-nm gap can separate two orthogonal polariza-

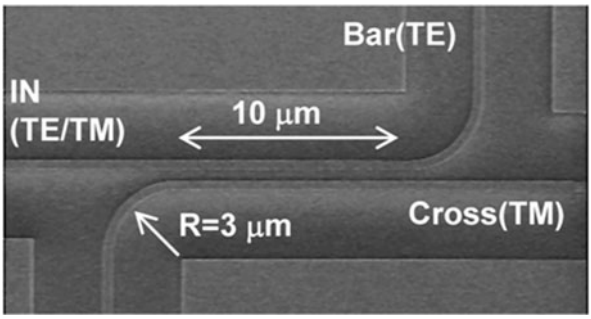

Fig. 1.28 A SEM image of the polarization splitter

tions through only a 10-μm-long propagation. For the suppression of additional coupling at the bending sections and for high-density integration, the ends of the coupler are tightly bent with a 3-μm radius. In the 200×400-nm^2 rectangular core, TE-like modes can propagate through the tight bend, but TM-like modes can not. Therefore, the exit waveguide for the TM-like modes is straight along the coupler.

The measured transmission of the splitter for various incident polarizations is shown in Fig. 1.29. The polarization was controlled by rotating a half-wave plate installed in front of the single-mode fiber for input. In the cross port, TM-like modes are dominant and TE modes are suppressed; in the bar port, vice versa. The maximum polarization extinction ratios (PERs) are 26 and 14 dB for bar and cross ports, respectively. Cascading two splitters improves the PER to about 23 dB for the cross port. A detailed study has shows that the applicable bandwidth is over 100 nm for a −10 dB PER [47].

A schematic of the fabricated rotator is shown in Fig. 1.30a [48]. The device has an off-axis double-core structure consisting of a 200-nm^2 silicon core, a 840-nm^2 silicon oxynitride (SiON) core, and a silica overcladding. The right and bottom edges of the thin silicon core overlap the corresponding edges of the second core. The SiON layer, with a refractive index of 1.60, and the silica layer are deposited by the PE–CVD method.

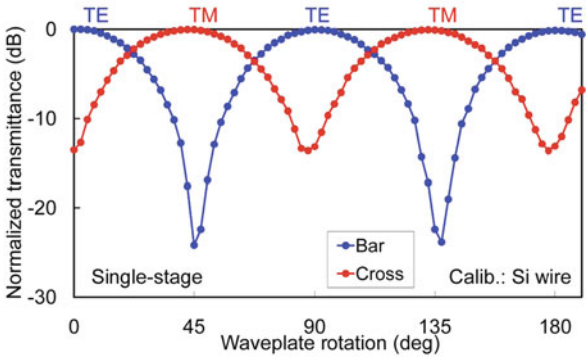

Fig. 1.29 Measured transmission of a single-stage polarization splitter for various incident polarizations

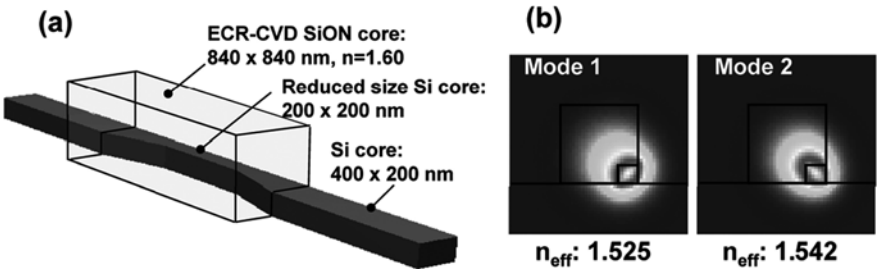

Fig. 1.30 (**a**) Schematic of the polarization rotation structure and (**b**) its eigenmodes

As shown in Fig. 1.30b, the double-core structure has two orthogonal eigenmodes with the eigenaxes tilted toward the substrate. Thus, propagation through the waveguide produces a rotation of the polarization plane when the polarization of incident light is just TE-like or TM-like modes. The polarization rotation angle is described by $\phi = \pi L \Delta n / \lambda$, where L is the propagation length, Δn the difference in the effective indices between two orthogonal eigenmodes, and λ the operation wavelength. The rotator length for 90° rotation $L_{\pi/2}$ is given by $\lambda / 2\Delta n$.

The measured output spectra for both polarization components of a 35-μm-long device are shown in Fig. 1.31a. Although the incident light has a TM-like component, the TM-like component after passing through the device is suppressed and the TE-like component becomes dominant. In other words, the incident TM component is converted into TE. The excess loss through the device is about 1 dB. The spectral ripples are caused by the polarization rotation in the normal silicon waveguides used for input and output, and they complicate the estimation of the actual rotation angle. A Poincare-mapping measurement gives a more accurate rotation angle and also the extinction ratio. As shown in Fig. 1.31b, the maximum rotation angle is 72°, and the maximum extinction ratio is about 11 dB, which is obtained for a 35-μm-long device [48].

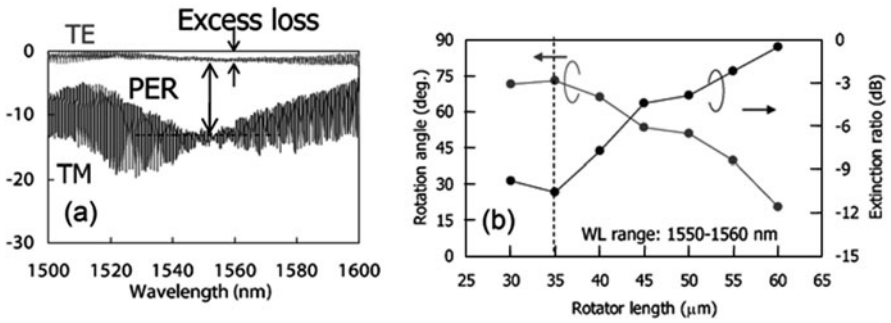

Fig. 1.31 (**a**) Measured transmission spectra of the polarization rotator with a length of 35 μm; (**b**) Polarization rotation angle estimated by the measured Poincare map and polarization extinction ratio calculated from the measured rotation angle

1.5.2 Polarization Diversity

A microscope image of the fabricated polarization diversity circuit is shown in Fig. 1.32 [46]. The circuit consists of polarization splitters, rotators, and a ring resonator wavelength filter with a 10-μm radius. The ring resonator has an extraordinary polarization dependence, which is shown in Fig. 1.15. In this diversity circuit, a splitter for the input separates the TE and TM components and feeds them into two waveguides. For the waveguide for the TM-like mode, the polarization is rotated into the TE-like mode. Thus, the polarization-dependent ring resonator can be used for both polarization inputs. There are two output waveguides for the ring resonator. In one of the waveguides, the TE-like mode is rotated into the TM-like mode and finally combined with another TE-like mode. In such a geometry, there is no PDλ, because this system uses only one functional device working for the TE mode. Moreover, the symmetry of the circuit eliminates the PDL and PMD originating from the normal waveguiding section [46]

Transmission spectra for wavelength filters with and without the polarization diversity are shown in Fig. 1.33. Without the diversity, the ring resonator works

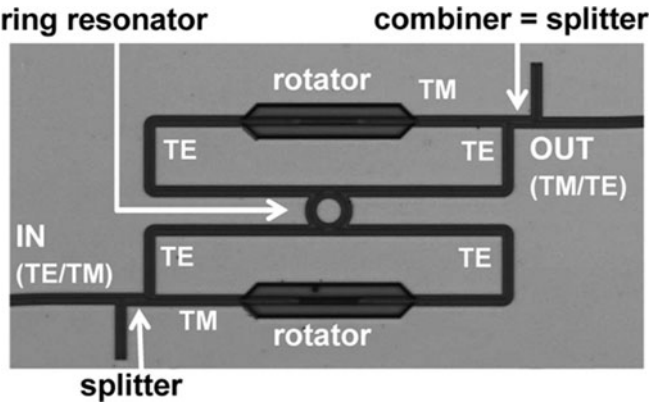

Fig. 1.32 Photograph of the polarization diversity circuit for a ring resonator filter

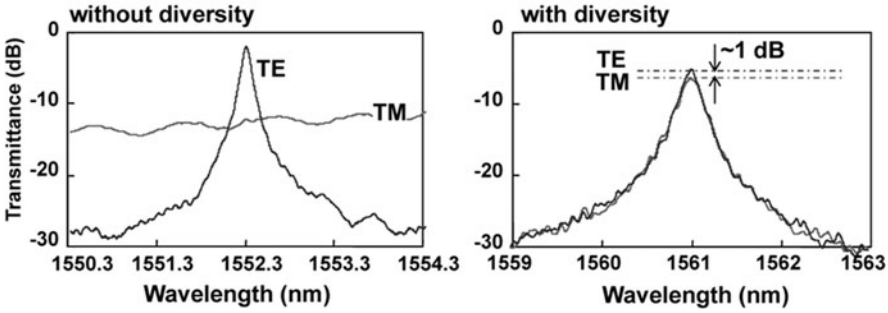

Fig. 1.33 Measured transmission spectra of a ring resonator with and without polarization diversity

as a fine wavelength filter for TE polarization, but it does not work at all for TM polarization. On the other hand, with polarization diversity, the circuit shows almost the same filter characteristics for both polarizations. The measured PDL of 1 dB is suitable for practical use.

1.6 Summary

Silicon photonic wire waveguides, featuring very strong optical confinement and compatibility with silicon electronics, provide us with a highly integrated platform for electronic–photonic convergence. The fundamental propagation performance of the waveguide has already become a practical standard. Some passive devices with sophisticated designs and dynamic devices with electronic structures have also been developed by using such waveguides. Moreover, the waveguide offers an efficient media for nonlinear optical functions. The polarization dependence, which is a serious obstacle to telecommunications applications, can be eliminated by using a monolithically integrated polarization diversity system.

In the next development stage, efforts will mainly shift to a large scale photonic integration in which passive, dynamic, and active devices will be integrated on a chip. The ultimate goal is, of course, a large-scale electronic–photonic integration, which is the most important advantage of the silicon photonic wire waveguide.

References

1. G.-L. Bona, R. Germann, B.J. Offrein, SiON high-refractive-index waveguide and planar lightwave circuits. IBM J. Res. Dev. **47**, 239–249 (2003) 2
2. M.J. Kobrinsky, B.A. Block, J.-F. Zheng, B.C. Barnett, R. Mohammed, M. Reshotko, F. Robertson, S. List, I. Young, K. Cadien, On-chip optical interconnects, Intel Technol. J. **8**, 129–141 (2004) 2
3. A.G. Rickman. G.T. Reed, F. Namavar, Silicon-on-insulator optical rib waveguide loss and mode characteristics. J. Lightwave Technol. **12**, 1771–1776 (1994) 2, 17
4. H. Rong, A. Liu, R. Jones, O. Cohen, D. Hak, R. Nicolaescu, A. Fang, M. Paniccia, An all-silicon Raman laser. Nature **433**, 292–294 (2005) 2, 20
5. K.K. Lee, D.R. Lim, H.-C. Luan, A. Agarwal, J. Foresi, L.C. Kimerling, Effect of size and roughness on light transmission in a Si/SiO2 waveguide: experiments and model. Appl. Phys. Lett. **77**, 1617–1619 (2000) 3
6. A. Sakai, G. Hara, T. Baba, Propagation characteristics of ultrahigh-Δ optical waveguide on silicon-on-insulator substrate. Jpn. J. Appl. Phys. **40**, L383–L385 (2001) 3, 14
7. K. Yamada, T. Tsuchizawa, T. Watanabe, J. Takahashi, E. Tamechika, M. Takahashi, S. Uchiyama, H. Fukuda, T. Shoji, S. Itabashi, H. Morita, Microphotonics devices based on silicon wire waveguiding system. IEICE Trans. Electron. **E87-C**, 351–358 (2004) 3, 14
8. T. Tsuchizawa, K. Yamada, H. Fukuda, T. Watanabe, J. Takahashi, M. Takahashi, T. Shoji, E. Tamechika, S. Itabashi, H. Morita, Microphotonics devices based on silicon microfabrication technology. IEEE J. Sel. Top. Quantum. Electron. **11**, 232–240 (2005) 3, 10
9. P. Dumon, W. Bogaerts, V. Wiaux, J. Wouters, S. Beckx, J.V. Campenhout, D. Taillaert, B. Luyssaert, P. Bienstman, D. Van Thourhout, R. Baets, Low-loss SOI photonic wires and ring resonators fabricated with deep UV lithography. Photon. Technol. Lett. **16**, 1328–1330 (2004) 3, 9

10. Y.A. Vlasov, S.J. McNab, Losses in single-mode silicon-on-insulator strip waveguides and bends. Opt. Express **12**, 1622–1631 (2004) 3, 13
11. T. Tsuchizawa, K. Yamada, H. Fukuda, T. Watanabe, S. Uchiyama, S. Itabashi, Low-loss Si wire waveguides and their application to thermooptic switches. Jpn. J. Appl. Phys. **45**, 6658–6662 (2006) 3, 10, 16
12. P. Lusse, P. Stuwe, J. Schule, H.-G Unger, Analysis of vectorial mode fields in optical waveguides by new finite difference method. J. Lightwave Technol. **LT-12**, 487–493 (1994) 4
13. M. Koshiba, S. Maruyama, K. Hirayama, A vector finite element method with the high-order mixed-interpolation-type triangular elements for optical waveguiding problems. J. Lightwave Technol. **LT-12**, 495–502 (1994) 4
14. A.S. Sudbo, Film mode matching: a versatile numerical method for vector mode field calculations in dielectric waveguides. Pure Appl. Opt. **2**, 211–233 (1993) 4
15. K. Okamoto, *Fundamentals of Optical Waveguides* (Academic Press, New York, 2000), p. 29 4
16. W. Bogaerts, P. Dumon, D. Van Thourhout, D. Taillaert, P. Jaenen, J. Wouters, S. Beckx, V. Wiaux, R. Baets, Compact wavelength-selective functions in silicon-on-insulator photonic wires. IEEE J. Sel. Top. Quantum. Electron. **12**, 1394–1401 (2006) 6, 14
17. F.P. Payne, J.P.R. Lacey, A theoretical analysis of scattering loss from planar optical wavewguide. Opt. Quantum. Electron. **26**, 977–986 (1994) 7
18. S. Janz, in *Silicon-Based Waveguide Technology for Wavelength Division Multiplexing*, ed. by L. Pavesi, D. Lockwood. Silicon Photonics. Top. Appl. Phys. 94 (Springer-Verlag, Berlin, 2004), p. 323 7
19. FIMMWAVE Software, Photon Design [Online]. Available: www.photond.com 7
20. T. Shoji, T. Tsuchizawa, T. Watanabe, K. Yamada, H. Morita, Low loss mode size converter from 0.3 μm square Si wire waveguides to single mode fibres. Electron. Lett. **38**, 1669–1670 (2002) 8, 20
21. Y. Hibino, Recent advances in high-density and large-scale AWG multi/demultiplexers with higher index-contrast silica-based PLCs. IEEE J. Sel. Top. Quantum. Electron. **8**, 1090–1101 (2002) 9
22. D. Taillaert, F. van Laere, M. Ayre, W. Bogaerts, D. van Thourhout, P. Bienstman, R. Baets, Grating couplers for coupling between optical fibers and nanophotonic waveguides. Jpn. J. Appl. Phys. **45**, 6071–6077 (2006) 9
23. T. Watanabe, K. Yamada, T. Tsuchizawa, H. Fukuda, H. Shinojima, S. Itabashi, Si wire waveguide devices. Proc. SPIE **6775**, 67750K (2007) 9
24. K.K. Lee, D.R. Lim, L.C. Kimerling, J. Shin, F. Cerrina, Fabrication of ultralow-loss Si/SiO_2 waveguides by roughness reduction. Opt. Lett. **26**, 1888–1890 (2001) 11
25. K. Yamada, T. Tsuchizawa, T. Watanabe, H. Fukuda, H. Shinojima, S. Itabashi, Fabrication and other related technologies for silicon photonic wire waveguides. Rev. Laser Eng. (in Japanese) **35**, 550–555 (2007) 14
26. F. Xia, M. Rooks, L. Sekaric, Y. Vlasov, Ultra-compact high order ring resonator filters using submicron silicon photonic wires for on-chip optical interconnects. Opt. Express **15**, 11934–11941 (2007) 14
27. F. Ohno, K. Sasaki, A. Motegi, T. Baba, Reduction in sidelobe level in ultracompact arrayed waveguide grating demultiplexer based on Si wire waveguide. Jpn. J. Appl. Phys. **45**, 6126–6131 (2006) 14
28. K. Yamada, T. Shoji, T. Tsuchizawa, T. Watanabe, J. Takahashi, S. Itabashi, Silicon-wire-based ultrasmall lattice filters with wide fre spectral ranges. Opt. Lett. **28**, 1663–1664 (2004) 14
29. K. Yamada, T. Tsuchizawa, T. Watanabe, J. Takahashi, H. Fukuda, M. Takahashi, T. Shoji, S. Uchiyama, E. Tamechika, S. Itabashi, H. Morita, Silicon wire waveguiding system: fundamental characteristics and applications. Electron. Commun. Jpn Part 2, **89**, 42–55 (2006) 14, 15
30. G. Cocorullo, I Rendina, Thermo-optical modulation at 1.5 μm in silicon etalon. Electron. Lett. 28, 83–85 (1992) 15
31. R. Kasahara, K. Watanabe, M. Itoh, Y. Inoue, A. Kaneko, Extremely low power consumption thermooptic switch (0.6 mW) with suspended ridge and silicon-silica hybrid waveguide structures. Proc 34th Eur. Conf. Opt. Commun. **5**, 55–56 (2008), Brussels 16, 17

32. R.A. Soref, B.R. Bennett, Electrooptical effects in silicon. IEEE J. Quantum Electron. **QE-23**, 123–129 (1987) 17
33. Q. Xu, B. Schmidt, S. Pradhan, M. Lipson, Micrometre-scale silicon electro-optic modulator, Nature **435**, 325–327 (2005) 17, 18
34. K. Yamada, T. Tsuchizawa, T. Watanabe, H. Fukuda, H. Shinojima, S. Itabashi, Applications of low-loss silicon photonic wire waveguides with carrier injection structures. Proc. 4th Intern. Conf. Group IV Photon., 116–118 (2007), Tokyo 17, 19
35. W.M.J. Green, M.J. Rooks, L. Sekaric, Y.A. Vlasov, Ultra-compact, low RF power, 10 Gb/s silicon Mach-Zehnder modulator. Opt. Express **15**, 17106–17113 (2007) 17, 18
36. H. Fukuda, K. Yamada, T. Shoji, M. Takahashi, T. Tsuchizawa, T. Watanabe, J.Takahashi, S. Itabashi, Four-wave mixing in silicon wire waveguides. Opt. Express **13**, 4629–4637 (2005) 20, 21
37. T.K. Liang, L.R. Nunes, T. Sakamoto, K. Sasagawa, T. Kawanishi, M. Tsuchiya, G.R.A. Priem, D. Van Thourhout, P. Dumon, R. Baets, H.K. Tsang, Ultrafast all-optical switching by crossabsorption modulation in silicon wire waveguides. Opt. Express **13**, 7298–7303 (2005) 20
38. K. Yamada, H. Fukuda, T. Tsuchizawa, T. Watanabe, T. Shoji, S. Itabashi, All-optical efficient wavelength conversion using silicon photonic wire waveguide. IEEE Photon. Technol. Lett. **18**, 1046–1048 (2006) 20, 21
39. M.A. Foster, A.C. Turner, J.E. Sharping, B.S. Schmidt, M. Lipson, A.L. Gaeta, Broad-band optical parametric gain on a silicon photonic chip. Nature **441**, 960–963 (2006) 20, 21
40. Q. Xu, R. Almeida, M. Lipson, Demonstration of high Raman gain in a submicrometer-size silicon-on-insulator waveguide. Opt. Lett. **30**, 35–37 (2005) 20
41. H. Takesue, H. Fukuda, T. Tsuchizawa, T. Watanabe, K. Yamada, Y. Tokura, S. Itabashi, Generation of polarization entangled photon pairs using silicon wire waveguide. Appl. Phys. Lett. **91**, 20118 (2007) 20
42. H. Takesue, H. Fukuda, T. Tsuchizawa, T. Watanabe, K. Yamada, Y. Tokura, S. Itabashi, Generation of polarization entangled photon pairs using silicon wire waveguide. Opt. Express **16**, 5721–5727 (2008) 20
43. K. Harada, H. Takesue, H. Fukuda, T. Tsuchizawa, T. Watanabe, K. Yamada, Y. Tokura, S. Itabashi, Generation of high-purity entangled photon pairs using silicon wire waveguide. Opt. Express **16**, 20368–20373 (2008) 20
44. O. Tadanaga, M. Asobe, H. Miyazawa, Y. Nishida, H. Suzuki, Efficient 1.55 μm-band quasi-phase-matched ZnO-doped LiNbO wavelength converter with high damage resistance. Electron. Lett. **39**, 1525–1575 (2003) 21
45. W. Bogaerts, D. Taillaert, P. Dumon, D. Van Thourhout, R. Baets, E. Pluk, A polarization-diversity wavelength duplexer circuit in silicon-on-insulator photonic wires. Opt. Express **15**, 1567–1578 (2007) 22
46. H. Fukuda, K. Yamada, T. Tsuchizawa, T. Watanabe, H. Shinojima, S. Itabashi, Silicon photonic circuit with polarization diversity. Opt. Express **16**, 4872–4880 (2008) 22, 25
47. H. Fukuda, K. Yamada, T. Tsuchizawa, T. Watanabe, H. Shinojima, S. Itabashi, Ultrasmall polarization splitter based on siliconwire waveguides. Opt. Express **14**, 12401–12408 (2006) 22, 23
48. H. Fukuda, K. Yamada, T. Tsuchizawa, T. Watanabe, H. Shinojima, S. Itabashi, Polarization rotator based on silicon wire waveguides. Opt. Express **16**, 2628–2635 (2008) 23, 24

Index